

Galactic Dust Polarization in Turbulent Multiphase ISM: On the Origin of the EE/BB Asymmetry

YUE HU* ,¹ BAO TRUONG ,^{2,3} THIEM HOANG ,^{2,3} AND LE NGOC TRAM ,⁴

¹*Institute for Advanced Study, 1 Einstein Drive, Princeton, NJ 08540, USA*

²*Korea Astronomy and Space Science Institute, Daejeon 34055, Republic of Korea*

³*Korea University of Science and Technology, 217 Gajeong-ro, Yuseong-gu, Daejeon, 34113, Republic of Korea*

⁴*Leiden Observatory, Leiden University, PO Box 9513, 2300 RA Leiden, The Netherlands*

ABSTRACT

Polarized thermal emission from Galactic dust is the dominant foreground for CMB polarization measurements at high frequencies, with its statistical properties set by the interplay between turbulence and magnetic fields in the multiphase interstellar medium (ISM). Variations in turbulence regime and density–magnetic-field alignment across the warm (WNM), unstable (UNM), and cold (CNM) neutral media should imprint distinct signatures on the power spectra and EE/BB power ratio, yet the relative phase contributions remain poorly constrained. Using high-resolution 3D magnetohydrodynamic simulations of a turbulent multiphase ISM coupled with synthetic dust polarization maps, we quantify phase-dependent turbulence, anisotropy, and alignment properties. We find that the trans-Alfvénic and transonic WNM and UNM are strongly anisotropic, exhibiting tight alignment of density and velocity structures with the local magnetic field. In contrast, the super-Alfvénic and supersonic CNM displays reduced anisotropy and weak alignment. These dynamical differences are reflected in the statistical scaling of fluctuations: the square root of the second-order velocity structure function exhibits a slope near $1/3$ in the WNM, near $1/2$ in the CNM, and intermediate in the UNM. Our synthetic observations reproduce the polarization power spectra measured by Planck. We find that polarization from UNM dust yields spectral indices most consistent with Planck, whereas WNM and CNM dust produce steeper and shallower spectra, respectively. The WNM yields $EE/BB > 2$, the UNM gives $EE/BB \sim 2$, and the CNM yields $EE/BB \approx 1$. These results indicate that UNM dust could be the dominant contributor to the polarized foreground. We present predictions at 150 GHz to improve foreground separation.

Keywords: Interstellar medium (847) — Neutral hydrogen clouds (1099) — Interstellar magnetic fields (845) — Interstellar dust (836) — Cosmic microwave background radiation (322)

1. INTRODUCTION

The interstellar medium (ISM) is a highly dynamic, multiphase environment where gas, dust, turbulence, and magnetic fields interact across a vast range of scales (McKee & Ostriker 1977; Wolfire et al. 1995; Stanimirovic et al. 1999; Vázquez-Semadeni et al. 2000; Lagache et al. 2000; Chepurnov & Lazarian 2010; Draine 2011; Lehner & Howk 2011; Crutcher 2012; Putman et al. 2012; Gray & Scannapieco 2017; Hu et al. 2019b, 2022; Liu et al. 2022; Ha et al. 2022; Tress et al. 2024; Vélguth et al. 2025; Hu et al. 2025a). Its multiphase nature plays a central role in key astrophysical processes, including cosmic ray propagation and acceleration (Jokipii 1966; Jokipii & Parker 1969; Qin et al. 2002; Xu & Lazarian 2020; Lazarian & Xu 2021; Hu et al. 2025c; Hopkins 2025), star formation (McKee & Ostriker 2007; Federrath & Klessen 2012; Crutcher 2012; Hu et al.

2019b, 2020; Federrath & Offner 2025; Vázquez-Semadeni 2025), and the evolution of galaxies (Scoville et al. 2017; Krumholz et al. 2018; Whittingham et al. 2023; Hu et al. 2025b). Of particular interest is the alignment of dust grains with magnetic fields, which leads to polarization of starlight and polarized thermal dust emission—a crucial probe of ISM magnetism and fundamental dust physics (Lazarian & Hoang 2007; Hoang & Lazarian 2008; Andersson et al. 2015; Hoang 2025).

This same polarized dust emission, however, also constitutes orders of magnitude the dominant Galactic foreground in measurements of cosmic microwave background (CMB) polarization (Ichiki 2014; BICEP2 Collaboration et al. 2014; Planck Collaboration et al. 2016a; Ade et al. 2019; Planck Collaboration et al. 2020, 2016b). At frequencies above 70 GHz, it poses a significant obstacle to detecting the faint primordial B -mode signal, widely regarded as a potential imprint of gravitational waves generated during cosmic inflation (Zaldarriaga 2001; Planck Collaboration et al. 2014a,b, 2015). A robust detection of such a signal would provide

compelling evidence for inflation and reveal new physics from the earliest moments of the Universe (Kamionkowski & Kovetz 2016; Ade et al. 2019).

Accurate removal of polarized Galactic foregrounds requires a physically grounded understanding of how magnetized interstellar structures give rise to the complex morphology and statistical properties of dust polarization observed across the sky (Kritsuk et al. 2018; Brandenburg et al. 2019; Huffenberger et al. 2020; McClure-Griffiths et al. 2023; Stalpes et al. 2024). Modeling the ISM, however, remains a major challenge: its highly compressible, multi-phase, and magnetized nature involves nonlinear and turbulent interactions spanning orders of magnitude in spatial scale (Stanimirovic et al. 1999; Vázquez-Semadeni et al. 2000; Kalberla & Kerp 2009; Draine 2011; Boulanger et al. 2018; Ho et al. 2024; Hu 2025; Vázquez-Semadeni 2025). It has been proposed that the alignment of dust filaments with the magnetic field generates the observed EE/BB asymmetry, in which the ratio of E -mode to B -mode power exceeds unity (Zaldarriaga 2001; Huffenberger et al. 2020). However, this alignment in the Galactic foreground, largely affected by MHD turbulence (Kandel et al. 2018), may vary between different ISM phases—the warm neutral medium (WNM), unstable neutral medium (UNM), and cold neutral medium (CNM). The relative contributions of these phases to the EE/BB asymmetry remain unexplored. As the fraction of WNM, UNM, and CNM varies across the sky (Kalberla & Kerp 2009; McClure-Griffiths et al. 2023), this knowledge is crucial for interpreting polarization measurements from upcoming CMB experiments.

In this study, we investigate foreground dust polarization using high-resolution (2048^3) 3D magnetohydrodynamic (MHD) simulations of the turbulent multiphase ISM. These simulations self-consistently evolve gas, turbulence, and magnetic fields across multiple thermal phases, capturing spatial scales from 100 pc down to 0.05 pc. Achieving such high resolution—thereby ensuring a broad inertial range—is essential to resolve both the large-scale driving of turbulence and the small-scale structures that shape the observed polarization. We explicitly examine the physical properties of the WNM, UNM, and CNM, as well as their alignment with the magnetic field.

Previous synthetic polarization studies based on MHD turbulence have typically relied on the assumption of uniform grain alignment and have not investigated the distinct contributions of different ISM phases (Planck Collaboration et al. 2015; Kritsuk et al. 2018; Ho et al. 2025). In this work, we generate synthetic dust polarization maps by post-processing our simulations with an upgraded version of the POLARIS code, which incorporates state-of-the-art grain alignment physics (Reissl et al. 2016; Giang et al. 2023). We also separate the contribution from WNM, UNM, and CNM. This allows us to quantify how the distinct phases of the ISM modulate key polarization properties, including the E - and B -mode power spectra and the EE/BB asymmetry. Such analysis is critical for refining foreground separation strategies in CMB experiments. Furthermore, we go beyond comparisons

with Planck observations at 353 GHz to present quantitative predictions for future CMB surveys at 150 GHz, establishing a physically motivated framework for the improved removal of polarized foregrounds in the search for primordial B -modes.

This paper is organized as follows. Section 2 describes the 3D multi-phase ISM simulations employed in this study and outlines the generation of synthetic dust polarization and the associated analysis methods. In Section 3, we present statistical analyses of the velocity, density, and magnetic field, followed by the statistics of dust polarization and the E - and B -mode power spectra. We conclude in Section 4 with a summary of the main results.

2. METHODOLOGY

2.1. MHD simulations of multi-phase ISM

The 3D multi-phase ISM simulations analyzed in this study were generated using the AthenaK code (Stone et al. 2024; Hu 2025). These simulations solve the ideal MHD equations with periodic boundary conditions, given by:

$$\begin{aligned} \frac{\partial \rho}{\partial t} + \nabla \cdot (\rho \mathbf{v}) &= 0, \\ \frac{\partial (\rho \mathbf{v})}{\partial t} + \nabla \cdot \left[\rho \mathbf{v} \mathbf{v}^T + \left(P + \frac{B^2}{8\pi} \right) \mathbf{I} - \frac{\mathbf{B} \mathbf{B}^T}{4\pi} \right] &= \mathbf{f}, \\ \frac{\partial \mathbf{B}}{\partial t} - \nabla \times (\mathbf{v} \times \mathbf{B}) &= 0, \\ \nabla \cdot \mathbf{B} &= 0, \\ \frac{\partial E}{\partial t} + \nabla \cdot \left[\mathbf{v} \left(E + P + \frac{B^2}{8\pi} \right) - \frac{\mathbf{B}(\mathbf{B} \cdot \mathbf{v})}{4\pi} \right] &= \Gamma - \Lambda, \end{aligned} \quad (1)$$

where P is the thermal pressure and \mathbf{f} is a stochastic forcing term applied to drive turbulence. The cooling rate, Λ , accounts for atomic line cooling and is parameterized as (Koyama & Inutsuka 2002):

$$\begin{aligned} \Lambda = \left(\frac{\rho}{m_H} \right)^2 \left[2 \times 10^{-19} \exp \left(\frac{-1.148 \times 10^5}{T + 1000} \right) \right. \\ \left. + 2.8 \times 10^{-28} \sqrt{T} \exp \left(\frac{-92}{T} \right) \right] \text{ erg s}^{-1} \text{ cm}^{-3}, \end{aligned} \quad (2)$$

where m_H is the hydrogen mass. The heating energy density rate, Γ , is given by:

$$\Gamma = \left(\frac{2\rho}{m_H} \right) \times 10^{-26} \text{ erg s}^{-1} \text{ cm}^{-3}. \quad (3)$$

We neglect thermal conduction, as its characteristic length scale ($\sim 10^{-2}$ pc) is subdominant on the large scales characteristic of the ISM (Vázquez-Semadeni et al. 2000; Ho et al. 2024).

The initial conditions consist of a uniform number density field $n = 1 \text{ cm}^{-3}$, corresponding to a mean column density $N_H = 3 \times 10^{20} \text{ cm}^2$, and a uniform magnetic field aligned along the z -axis. We adopt a field strength of $B \approx 3 \mu\text{G}$,

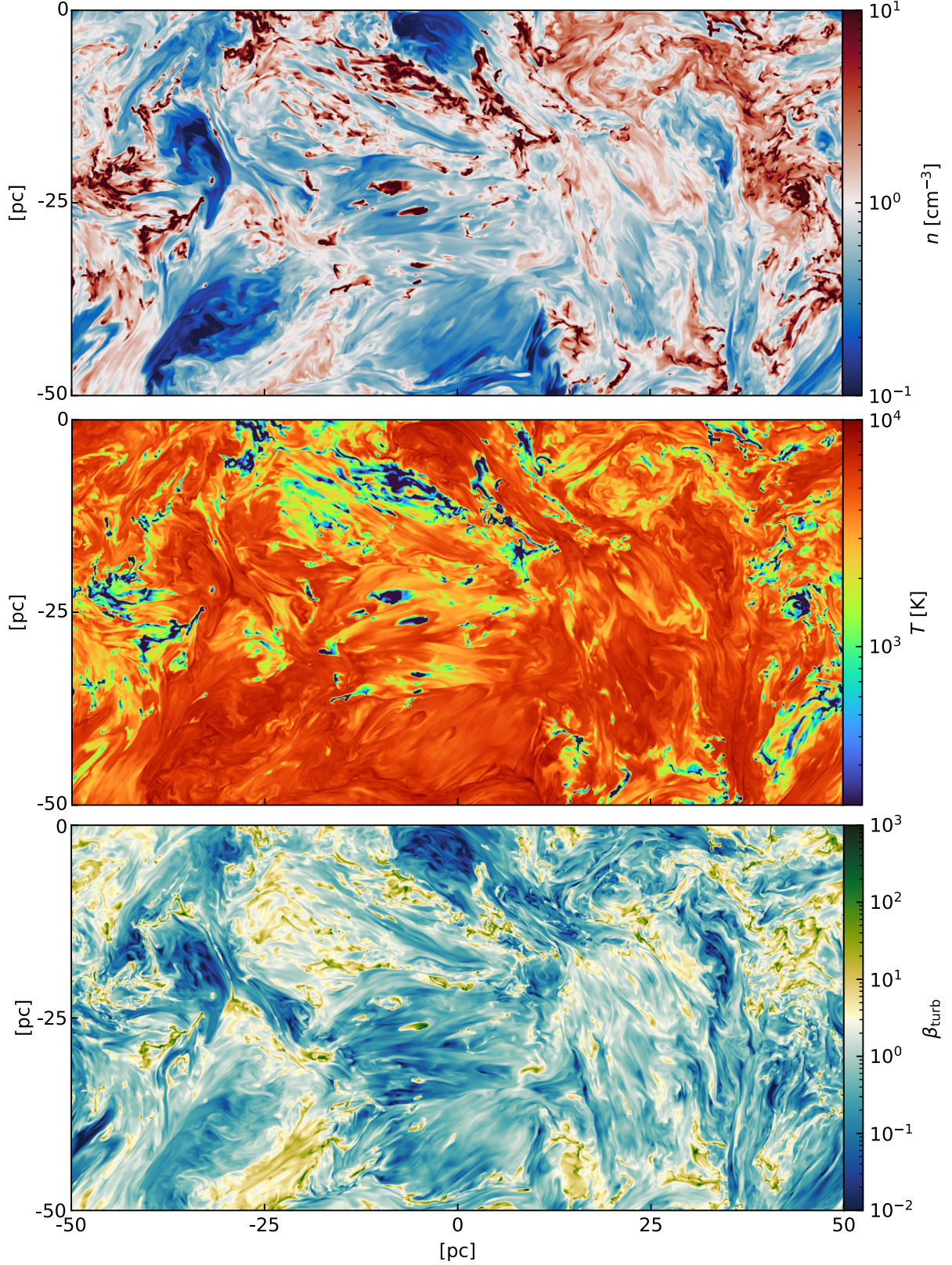


Figure 1. Distributions of number density n , temperature T , and turbulent plasma beta β_{turb} in the multiphase ISM simulation. Shown is a two-dimensional slice from the 2048^3 simulation, displaying the number density (top), temperature (middle), and turbulent plasma beta $\beta_{\text{turb}} = \rho v^2 / (B^2 / 8\pi)$ (bottom), where ρ is the gas mass density and v is the local turbulent velocity. For visualization purposes, only half of each slice is shown. The cold neutral medium, characterized by low temperature, is spatially correlated with the densest regions.

consistent with Zeeman observations (Crutcher 2012). The velocity dispersion is initialized at $\sigma_v \approx 10 \text{ km s}^{-1}$, based on Larson's law and observational constraints derived from young stellar environments (Larson 1981; Ha et al. 2022).

The simulation box spans 100 pc. Turbulence is driven solenoidally at an injection scale of $L_{\text{inj}} = 50 \text{ pc}$, corresponding to a peak wavenumber of $k = 1/L_{\text{inj}} = 0.02 \text{ pc}^{-1}$. The computational domain is discretized on a uniform 2048^3 grid and the effective numerical dissipation scale is approximately 10 cells. The simulations are evolved for 100 Myr to ensure turbulence reaches a steady state.

2.2. Synthetic dust polarization maps

We use the updated POLARIS code from Giang et al. (2023), incorporating modern physics of grain alignment by radiative torques (RATs) to post-process our MHD simulation. For dust properties, we consider interstellar dust following the Astrodust model (i.e., silicate and carbonaceous components are mixed in one single grain population, see Draine & Hensley 2021). We use the oblate spheroidal shape of axial ratio $s = 1.4$, and the optical constant from the Astrodust model, which was previously constrained from ISM polarimetric observations by Hensley & Draine (2023). The grain size distribution is assumed to follow the MRN power law (Mathis et al. 1977) of $dn/da = Ca^{-3.5}$, where C is the normalization constant derived from the dust-to-gas mass ratio of 0.01 and the grain sizes span from the minimum size of $a_{\text{min}} = 0.005 \mu\text{m}$ to the maximum size $a_{\text{max}} = 0.25 \mu\text{m}$ in the diffuse ISM (Mathis et al. 1977). The dust composition and size distribution are considered to be uniform across multi-phase ISM components.

For the dust heating and cooling process, we assume that dust grains are irradiated by the standard diffuse interstellar radiation field (ISRF) from Mathis et al. (1983) and reemit infrared emission that depends on the dust temperature and optical properties. The dust temperature is calculated in POLARIS using Monte Carlo radiative transfer (Reissl et al. 2016). The dust grain equilibrium temperature is $T_d \sim 18 - 20 \text{ K}$ in WNM/UNM with $n < 10 \text{ cm}^{-3}$, and it decreases slightly to $T_d \sim 16 \text{ K}$ in CNM with $n \sim 10 - 100 \text{ cm}^{-3}$ because of ISRF attenuation.

For grain alignment physics, we consider the ideal RAT model in which dust grains are aligned with the ambient magnetic field by RATs from the ISRF. All grains larger than the critical alignment size, a_{align} , are perfectly aligned by RATs (Hoang & Lazarian 2008). This ideal RAT model is achieved for superparamagnetic grains containing embedded iron clusters in the ISM (Lazarian & Hoang 2007; Hoang & Lazarian 2016; Hoang 2025). The calculation of grain alignment properties is incorporated in the latest version of the POLARIS code (Giang et al. 2023). For the multi-phase ISM with $n < 100 \text{ cm}^{-3}$, the magnetic alignment by RATs is efficient with small $a_{\text{align}} \sim 0.01 - 0.05 \mu\text{m}$ and high average alignment efficiency $\langle f_{\text{align}} \rangle \sim 0.7 - 0.8$ (Hoang & Truong 2024). The fluctuation in the dust polarization is then mainly attributed to the density and magnetic fluctuation effects across ISM-phase components.

Given dust physical (size distribution, shape, and composition) and grain alignment properties, POLARIS solves the polarized radiative transfer in to generate the synthetic thermal dust polarization map at 353 GHz and 150 GHz. For this paper, we analyze the synthetic polarization angles and quantify E/B modes. In the follow-up paper, we will study in detail the effects of multi-phase ISM and magnetic turbulence on the synthetic polarization fraction. For more details of the implementations of grain alignment physics and polarized radiative transfer in the POLARIS code, please see, e.g., Reissl et al. (2016); Giang et al. (2023); Truong & Hoang (2025).

2.3. Structure function

We utilize the second-order structure function, a widely accepted method for quantifying the statistical properties of turbulent flows. The structure function of velocity is defined as:

$$D_v(r) = \langle |\mathbf{v}(\mathbf{x} + \mathbf{r}) - \mathbf{v}(\mathbf{x})|^2 \rangle_r, \quad (4)$$

where $\mathbf{v}(\mathbf{x})$ is the velocity at position \mathbf{x} , and \mathbf{r} represents the separation vector. This function can be adapted to measure magnetic field or gas density fluctuations by replacing $\mathbf{v}(\mathbf{x})$ with $\mathbf{B}(\mathbf{x})$ or $n(\mathbf{x})$, respectively. In the following, we will add the subscripts “ v ”, “ B ”, or “ n ” to $D(r)$ for distinguishing velocity, magnetic field, and number density accordingly.

To investigate the anisotropy in turbulence within our simulations, we decompose the structure-function into components parallel and perpendicular to the local magnetic fields, following the methodology described in Cho & Vishniac (2000):

$$\begin{aligned} \mathbf{B}' &= \frac{1}{2}(\mathbf{B}(\mathbf{x} + \mathbf{r}) + \mathbf{B}(\mathbf{x})), \\ D_v(R, z) &= \langle |\mathbf{v}(\mathbf{x} + \mathbf{r}) - \mathbf{v}(\mathbf{x})|^2 \rangle_r, \end{aligned} \quad (5)$$

where \mathbf{B}' defines the local magnetic field direction in a cylindrical coordinate system, with z -axis parallel to \mathbf{B}' , $R = |\hat{z} \times \mathbf{r}|$ and $z = \hat{z} \cdot \mathbf{r}$, where $\hat{z} = \mathbf{B}'/|\mathbf{B}'|$.

From these, we can derive the parallel (δv_{\parallel}) or perpendicular (δv_{\perp}) velocity fluctuations relative to the local magnetic fields as follows:

$$\begin{aligned} \delta v_{\perp} &= \sqrt{D_v^{\perp}} = \sqrt{D_v(R, 0)}, \\ \delta v_{\parallel} &= \sqrt{D_v^{\parallel}} = \sqrt{D_v(0, z)}. \end{aligned} \quad (6)$$

Similarly, the parallel (δB_{\parallel}) or perpendicular (δB_{\perp}) magnetic field fluctuations are obtained from:

$$\begin{aligned} \delta B_{\perp} &= \sqrt{D_B^{\perp}} = \sqrt{D_B(R, 0)}, \\ \delta B_{\parallel} &= \sqrt{D_B^{\parallel}} = \sqrt{D_B(0, z)}. \end{aligned} \quad (7)$$

3. RESULTS

3.1. Turbulent and multiphase nature of the ISM

Traditionally, the ISM is modeled as a multiphase medium in approximate pressure equilibrium, comprising a warm,

diffuse component with temperatures $T > 5000$ K (i.e., WNM); an intermediate-density, thermally unstable component with $200 < T < 5000$ K (i.e., UNM); and a cold, dense component with $T < 200$ K (i.e., CNM) (McKee & Ostriker 1977; Wolfire et al. 2003; Draine 2011). This multiphase structure is illustrated in Fig. 1, which displays 2D cross-sections of the number density, temperature, and velocity fields. These snapshots correspond to typical ISM conditions, characterized by a turbulent velocity dispersion of $\sigma_v \approx 10 \text{ km s}^{-1}$ and a mean magnetic field strength of $B_0 \approx 3 \mu\text{G}$.

3.1.1. Thermal, kinetic, and magnetic field energy budget

Turbulence induces significant fluctuations in density, temperature, and velocity throughout the ISM. In particular, turbulent mixing plays a crucial role in redistributing energy and sustaining the UNM, while thermal instability acts as a secondary contributor (Vázquez-Semadeni et al. 2000; Ho et al. 2024; Hu 2025). The interplay between turbulent mixing and magnetic fields—both of which support the intermediate phase—results in mass fractions of 21.79% for the CNM, 33.93% for the WNM, and 44.28% for the UNM. The mass fractions are consistent with the multi-phase ISM in high latitude $|b| > 30^\circ$ regions (Kalberla & Haud 2018), which are the major targets for the foreground polarization subtraction (Planck Collaboration et al. 2016a).

The relative importance of thermal pressure and magnetic forces is characterized by the thermal plasma beta, $\beta_{\text{th}} = (\rho c_s^2 / \gamma) / (B^2 / 8\pi)$, where c_s is the sound speed. As shown in Fig. 2 and summarized in Table 2, β_{th} in the WNM and UNM spans a broad range from 10^{-1} to 10^2 , with a median value ~ 0.7 . In contrast, the CNM exhibits a narrower distribution (10^{-1} to 10^1) with a lower median of 0.4. Dynamically, the WNM and UNM are transonic, with median sonic Mach numbers (M_s) of 1.1–1.5. The CNM, however, is highly supersonic with a median $M_s \approx 6.6$, indicating that shock compression plays an important role in shaping this cold phase.

To quantify the balance between turbulent kinetic energy and magnetic energy, we examine the turbulent plasma beta, $\beta_{\text{tur}} = \rho v^2 / (B^2 / 8\pi) = 2M_A^2$, where M_A is the Alfvén Mach number. In the WNM and UNM, β_{tur} ranges from 10^{-2} to 10^2 with median values between 1.4 and 2.8. This indicates that these phases are generally in a trans-Alfvénic state where magnetic and turbulent kinetic energies are comparable, although local conditions may vary. Conversely, the CNM is characterized by super-Alfvénic (i.e., $\beta_{\text{tur}} > 2$ or $M_A > 1$) turbulence; with a median $\beta_{\text{tur}} \approx 40$, the turbulent kinetic energy significantly dominates, rendering the magnetic field dynamically subdominant.

The super-Alfvénic nature of the CNM is consistent with turbulent dynamo theory. Assuming the largest scale of a CNM cloud is ~ 10 pc, the dynamo saturation timescale is estimated to exceed ten large-scale eddy turnover times, i.e., $t_{\text{dyn}} \sim 10t_{\text{eddy}} \sim 20$ Myr. The supersonic CNM is also affected by shock compression that operates on a shorter timescale of $t_{\text{comp}} \sim 2$ Myr. However, turbulent mixing oc-

fers rapidly with its rate determined by the smallest scales ($t_{\text{mix}} \sim 0.3$ Myr at the ~ 0.5 pc dissipation scale). It acts to disrupt the compression process. Consequently, these dynamic timescales are significantly shorter than the dynamo saturation timescale, so that the turbulent kinetic energy thus consistently exceeds the magnetic energy. This dominance of turbulence suggests that the magnetic field within the CNM is highly stochastic and passively tangled by the turbulent motions.

3.1.2. Parallel alignment of density, velocity, and magnetic field structures with the local magnetic field

The variation in the energy partition between turbulence and magnetic fields profoundly influences the geometric alignment of ISM structures. In transonic (or subsonic) compressible MHD turbulence, the turbulent cascade proceeds preferentially in the perpendicular direction, promoting the mixing of density fluctuations into elongated filaments aligned parallel to the local magnetic field. The aspect ratio of these filaments is governed by the degree of turbulence anisotropy (Xu et al. 2019) and modulated by phase transition processes (Ho et al. 2023). Conversely, in the super-Alfvénic and supersonic regimes, the magnetic field is dynamically subdominant. Here, isotropic shock compression becomes the primary shaping mechanism, capable of generating density structures oriented perpendicular to the magnetic field, e.g., in post-shock layers (Xu et al. 2019; Hu et al. 2019a; Beattie & Federrath 2020).

In Fig. 2, we quantify this alignment using the relative angles θ_ρ , θ_v , and θ_B . These are defined as the angles between the local magnetic field and the vectors perpendicular to the gradients $\nabla\rho$, ∇v , and ∇B (i.e., the gradients rotated by 90°). The gradients are calculated at the cell scale (~ 0.05 pc). This rotation ensures that the angles represent the orientation of the structure's elongation relative to the local magnetic field: $\theta \approx 0^\circ$ indicates parallel alignment (structures aligned with B), while $\theta \approx 90^\circ$ indicates perpendicularity.

The distributions of θ_ρ reveal distinct phase-dependent behaviors (see Fig. 2), while all distributions peak at zero. θ_ρ in WNM has the least dispersed distribution, indicating the most pronounced parallel alignment. This is typically characterized by trans-Alfvénic and transonic conditions favorable for anisotropic MHD cascading. The UNM shows intermediate alignment, while the super-Alfvénic and supersonic CNM exhibits significantly weaker parallel alignment, i.e., broader distribution. This trend confirms theoretical expectations: as the Mach number increases and the Alfvénic constraint weakens, supersonic shocks disrupt the field-aligned anisotropy, introducing a population of shock-compressed structures perpendicular to the field (Xu et al. 2019; Hu et al. 2019a; Beattie & Federrath 2020; Ho et al. 2023). This phase-dependent density structural alignment has direct consequences for the polarization statistics discussed in § 3.3. The strong parallel alignment in the trans-Alfvénic WNM and UNM effectively projects power into the E -mode, enhancing the E -mode and B -mode's power spec-

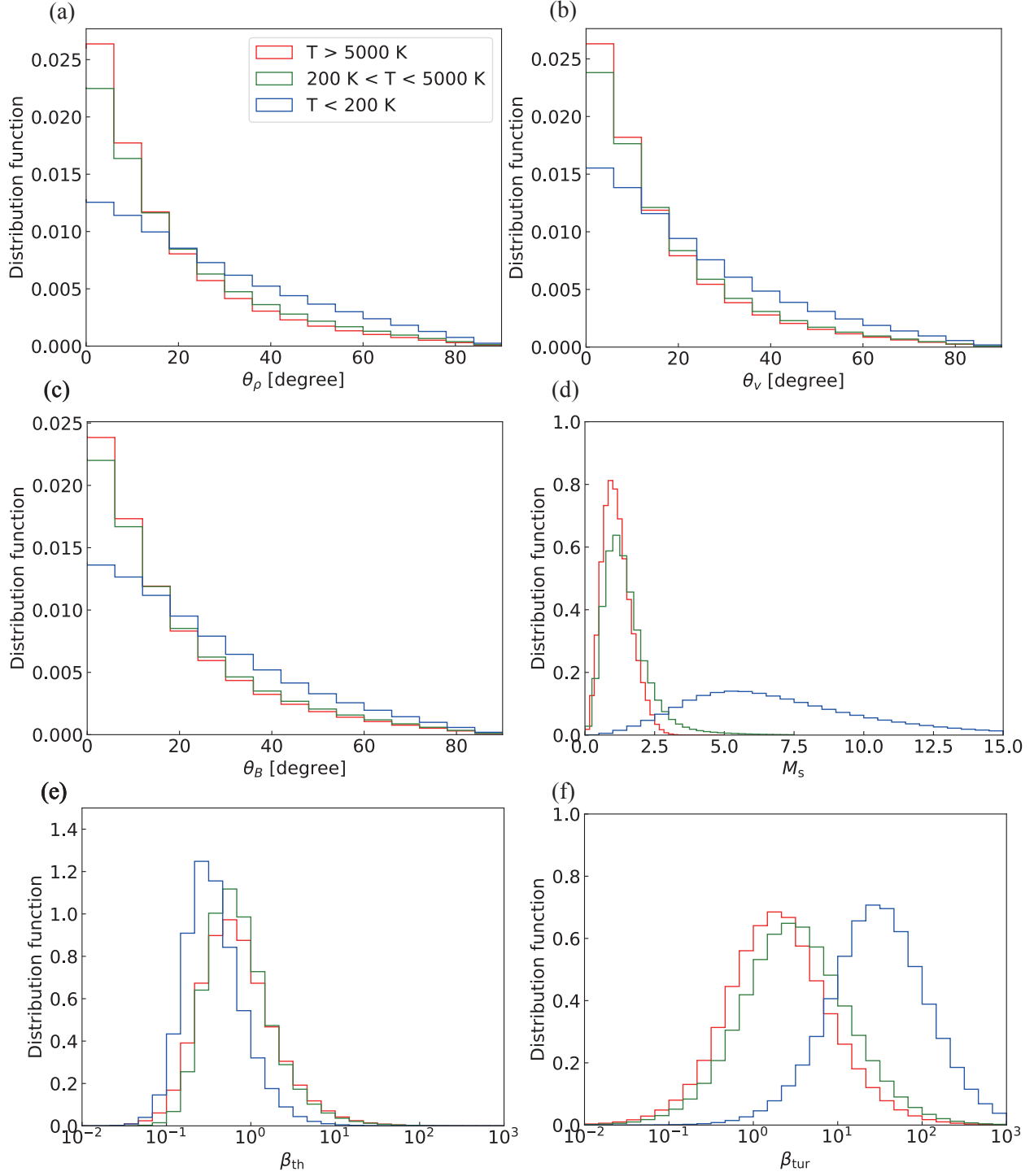


Figure 2. Panels (a), (b), and (c): Distributions of the relative angle θ_ρ , θ_v , and θ_B between the local magnetic field and the rotated (by 90 degrees) density gradient $\nabla\rho$, velocity gradient ∇v , and magnetic field strength gradient ∇B , respectively. The relative angles are evaluated separately for the warm neutral medium (WNM; $T > 5000$ K), unstable neutral medium (UNM; $200 \text{ K} < T < 5000$ K), and cold neutral medium (CNM; $T < 200$ K). Here, a relative angle of 0° corresponds to parallel alignment, while 90° indicates perpendicularity. **Panel (d):** Distribution of the sonic Mach number $M_s = v/c_s$ in each phase. **Panel (e):** Distribution of the thermal plasma beta, $\beta_{th} = (\rho c_s^2/\gamma)/(B^2/8\pi)$. **Panel (f):** Distribution of the turbulent plasma beta, $\beta_{tur} = \rho v^2/(B^2/8\pi)$. All quantities are phase-separated based on temperature and computed in three dimensions.

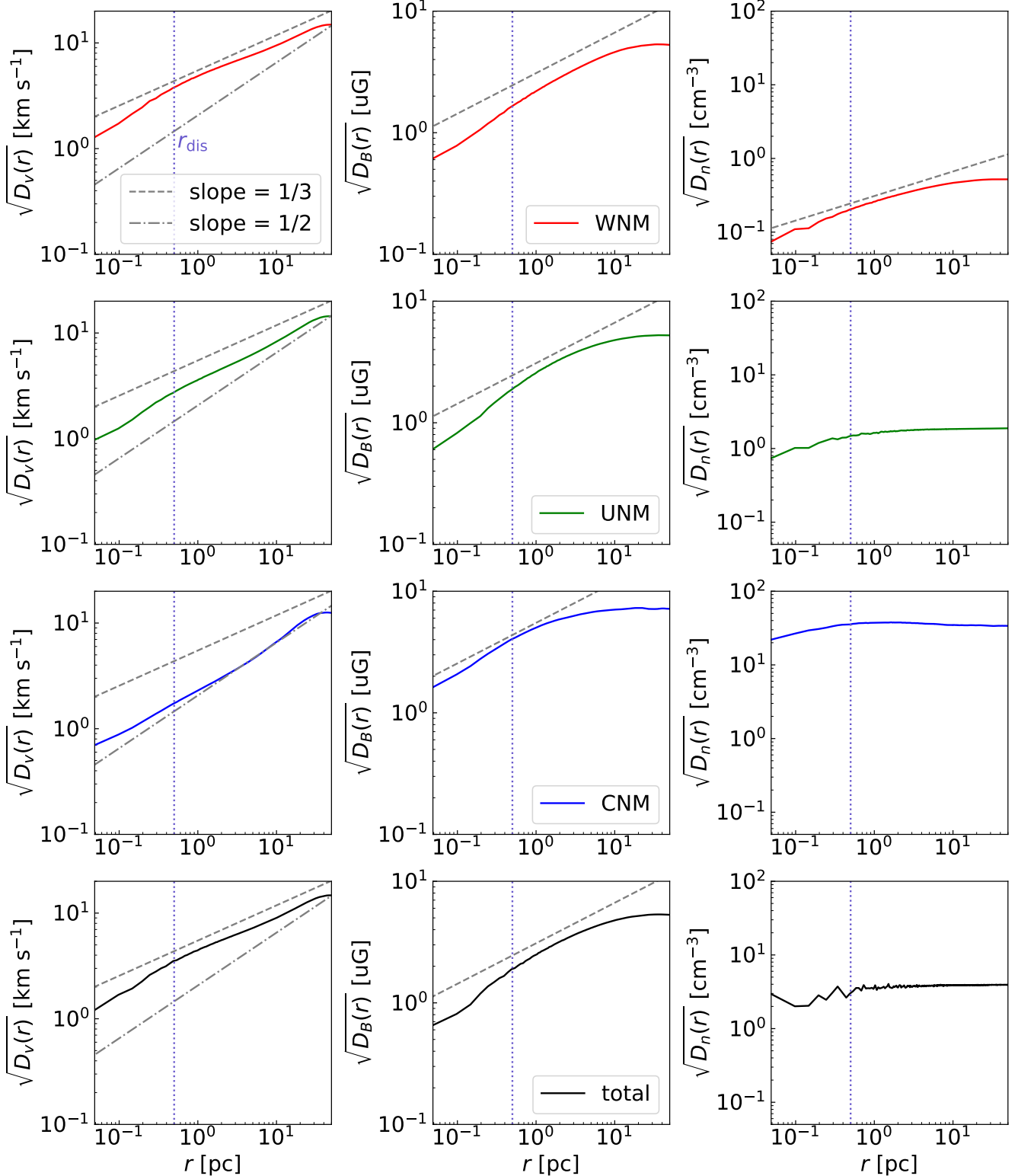


Figure 3. Statistical properties of scale-dependent fluctuations of velocity (1st column), magnetic field (2nd column), and number density (3rd column) in different ISM phases. The fluctuations are computed as the square root of the second-order structure function for each quantity, shown separately for the WNM ($T > 5000$ K), UNM (200 K $< T < 5000$ K), CNM ($T < 200$ K), and the total ISM (including all phases). Dashed and dash-dotted reference lines indicate slopes of $1/3$ and $1/2$, corresponding to Kolmogorov and Burgers turbulence scaling, respectively. The numerical dissipation scale r_{dis} is around 0.5 pc.

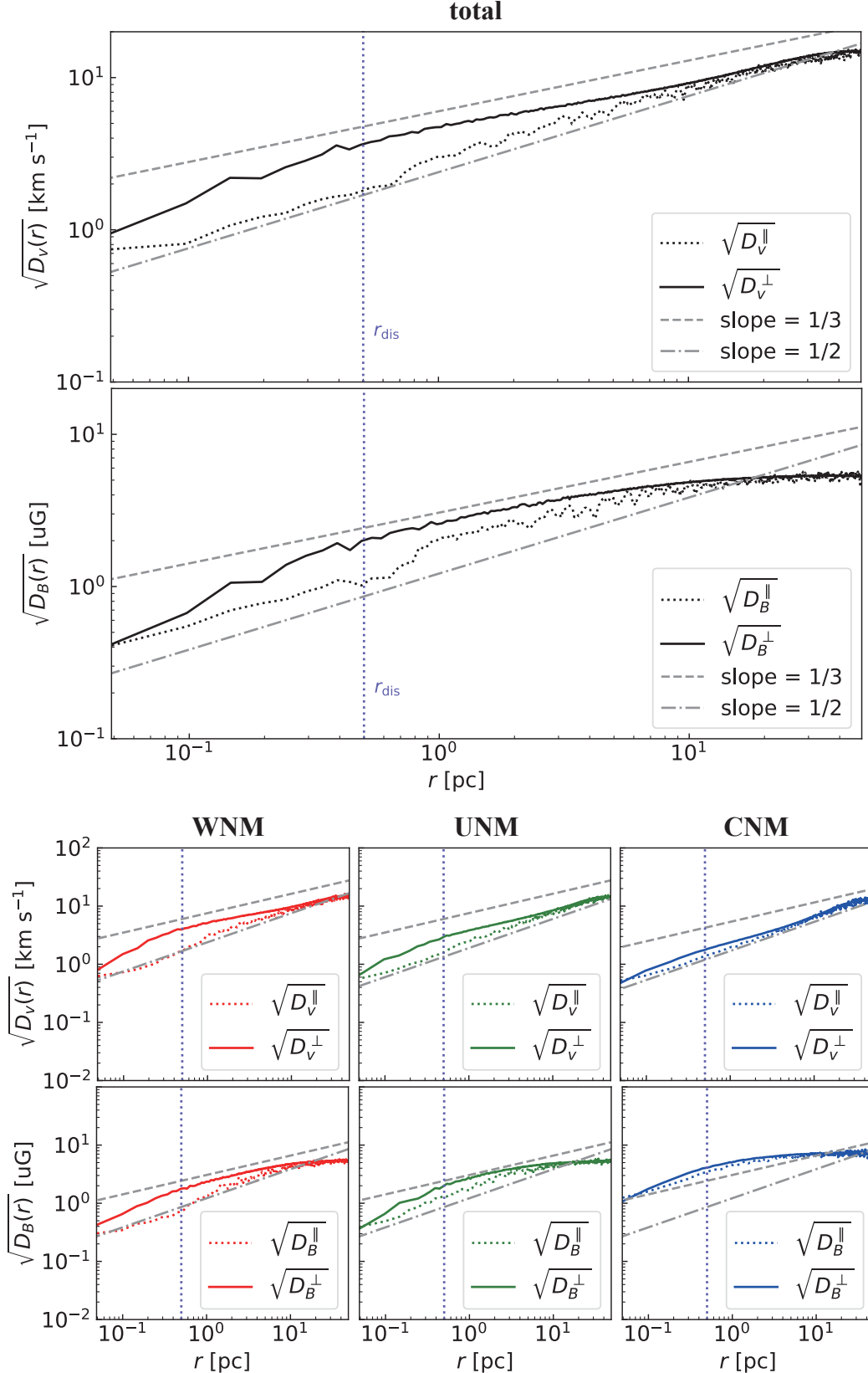


Figure 4. Statistical properties of scale-dependent velocity and magnetic field fluctuations decomposed into components parallel and perpendicular to the local magnetic field in different ISM phases. Fluctuations are computed as the square root of the second-order structure function. They are shown separately for the WNM, UNM, CNM, and the total ISM (including all phases). Dashed and dash-dotted grey lines represent reference slopes of 1/3 and 1/2, corresponding to Kolmogorov and Burgers turbulence scalings, respectively. The numerical dissipation scale r_{dis} is around 0.5 pc.

tral ratio. In contrast, the randomization of structure orientation (or tendency toward perpendicularity) in the shock-dominated CNM reduces the geometric anisotropy, expected to drive the EE/BB ratio closer to unity.

The distributions of θ_v and θ_B are similar to that of θ_ρ , showing strong parallel alignment with the local magnetic field. This demonstrates the physical foundations of using velocity gradient (Lazarian & Yuen 2018; Hu et al. 2018) and synchrotron intensity gradient (Lazarian et al. 2017; Hu et al. 2024) to trace the magnetic field in diffuse ISM.

3.2. Statistics of velocity, magnetic field, and density fluctuations

Fig. 3 presents the square root of the undecomposed second-order structure functions for velocity, magnetic field, and density. The quantitative power-law slopes α fitted in the inertial range (0.5 – 10 pc) are summarized in Table 1.

For velocity, the WNM exhibits a power-law slope of $\alpha_v \approx 0.29$, which is slightly shallower than the standard Kolmogorov turbulence scaling (1/3). This slope progressively steepens in the denser phases. In the UNM, the slope increases to $\alpha_v \approx 0.36$. In the CNM, the slope reaches $\alpha_v \approx 0.46$, closely approaching the value of 1/2 indicative of Burgers turbulence (shock-dominated). While this steepening in the CNM is typically attributed to the presence of supersonic shocks ($M_s \approx 6.6$) that efficiently dissipate kinetic energy, Hu (2025) found that similar steepening can occur in the subsonic WNM under hydrodynamical conditions. This suggests that phase transition dynamics may also play a role in modifying the energy cascade. Finally, the velocity structure function of the total ISM ($\alpha_v \approx 0.30$) closely mirrors that of the volume-filling WNM ($\alpha_v \approx 0.29$), indicating that the WNM dominates the global turbulent velocity statistics.

For the magnetic field structure function, the WNM exhibits a slope of $\alpha_B \approx 0.33$, perfectly consistent with Kolmogorov scaling. The UNM shows a slightly shallower slope of $\alpha_B \approx 0.28$. In contrast, the CNM displays a significantly shallower magnetic field slope of $\alpha_B \approx 0.15$. This low value, combined with the flattening observed at scales above 5 pc, suggests that the magnetic field becomes uncorrelated at larger scales within the clumpy cold medium. Despite the high amplitude of fluctuations in the CNM, the structure function of the total ISM ($\alpha_B \approx 0.29$) closely tracks the WNM and UNM values. This implies that, while the CNM contains intense local fluctuations, the globally volume-filling WNM and UNM govern the overall magnetic field statistics of the ISM.

Regarding the density structure function, the UNM and CNM lack a clear power-law scaling. Their slopes are close to zero ($\alpha_n \approx 0.05$ for UNM and $\alpha_n \approx -0.03$ for CNM), indicating that the correlation of density fluctuations in these phases is insignificant and power is concentrated at small scales. The WNM, despite having a lower mean density, exhibits a discernible—albeit shallow—power-law trend with $\alpha_n \approx 0.26$. Notably, unlike the velocity and magnetic field statistics, the density structure function of the total ISM is

nearly flat ($\alpha_n \approx 0.04$) and is dominated by the contributions from the dense UNM and CNM phases.

3.2.1. Anisotropy of the multi-phase ISM

As shown in Section 3.1.2, the gradients of density, velocity, and magnetic field—when rotated by 90°—are preferentially aligned parallel to the local magnetic field direction. This confirms that the underlying physical density, velocity, and magnetic field structures are themselves elongated parallel to the local magnetic field. Such MHD turbulence anisotropy has profound implications for the alignment, especially between density structures and the magnetic field. In subsonic and transonic compressible MHD turbulence, the turbulent cascade develops preferentially in directions perpendicular to the magnetic field. This anisotropic mixing promotes the formation of elongated density structures that align parallel to the local magnetic field lines (Xu et al. 2019). It consequently can regulate polarization statistics, such as the EE/BB ratio (Kandel et al. 2018).

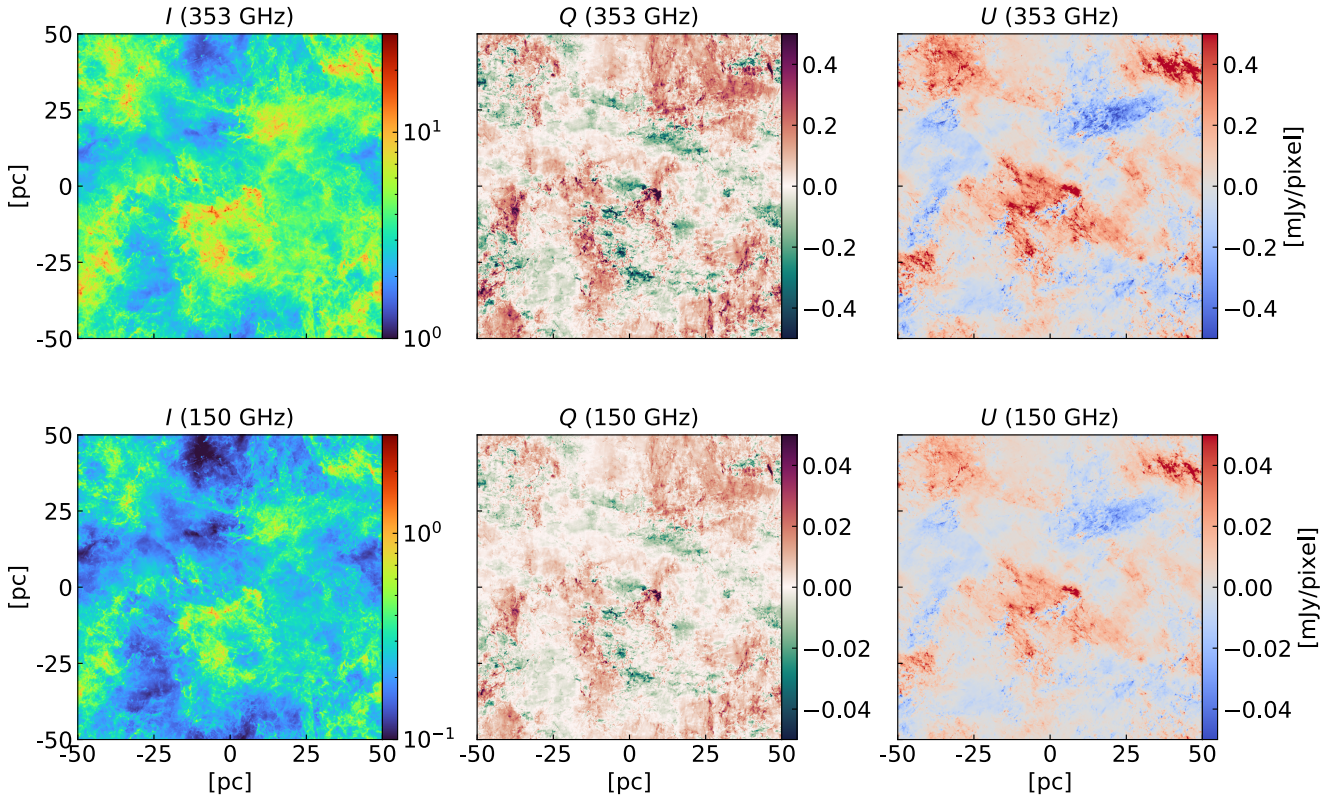
In Fig. 4, we quantify this anisotropy by decomposing the square root of the second-order velocity structure function into components parallel (\parallel) and perpendicular (\perp) to the local magnetic field. For the total velocity field, the perpendicular component exhibits a slope of $\alpha_{v,\perp} = 0.29$, close to the Kolmogorov scaling, while the parallel component scales with a slope of $\alpha_{v,\parallel} = 0.47$ (see Table 1). Crucially, the velocity anisotropy—defined as the ratio of these components—is scale-dependent and becomes more pronounced at smaller scales, consistent with theoretical expectations for magnetized turbulence (Lazarian & Vishniac 1999; Cho & Vishniac 2000; Hu et al. 2021).

Phase decomposition reveals that the perpendicular component dominates the power across most scales in the diffuse phases, converging with the parallel component only at the driving scale (~ 50 pc). This anisotropy is most prominent in the WNM and UNM. In the WNM, the perpendicular velocity slope is $\alpha_{v,\perp} = 0.27$, while the parallel component reaches $\alpha_{v,\parallel} = 0.48$. The UNM shows a similar trend with $\alpha_{v,\perp} = 0.34$ and $\alpha_{v,\parallel} = 0.49$. In contrast, the super-Alfvénic CNM exhibits nearly isotropic scaling, with both perpendicular ($\alpha_{v,\perp} = 0.45$) and parallel ($\alpha_{v,\parallel} = 0.52$) components approaching the 1/2 slope. Analysis of the magnetic field structure functions (Fig. 4) shows analogous behavior. The perpendicular magnetic component generally dominates, scaling with a total slope of $\alpha_{B,\perp} = 0.26$, though this value reaches $\alpha_{B,\perp} = 0.31$ in the WNM up to a phase-dependent saturation scale. Beyond this scale—approximately 8 pc in the WNM, 5 pc in the UNM, and 1 pc in the CNM—the slope flattens, indicating reduced correlation in the magnetic fluctuations. The parallel magnetic component in the WNM exhibits a slope of $\alpha_{B,\parallel} = 0.49$, whereas it flattens significantly in the UNM (0.37) and CNM (0.19). For both velocity and magnetic fields, the perpendicular-to-parallel ratio reaches a factor of ~ 3 at the dissipation scale (0.5 pc) in the WNM and UNM, while remaining notably lower (~ 1.25) in the CNM.

Table 1. Properties of the square root of the second-order structure function in the Multi-phase Medium

Phase	$f_{\text{mass}} (\%)$	$f_{\text{vol}} (\%)$	Slope α_n	Slope α_v			Slope α_B		
				Tot.	Tot.	\parallel	Tot.	\parallel	\perp
						\perp			
Total	100	100	0.04	0.30	0.47	0.29	0.29	0.40	0.26
WNM	33.93	61.04	0.26	0.29	0.48	0.27	0.33	0.49	0.31
UNM	44.28	38.01	0.05	0.36	0.49	0.34	0.28	0.37	0.26
CNM	21.79	0.95	-0.03	0.46	0.52	0.45	0.15	0.19	0.15

Notes. Columns list the mass fraction (f_{mass}), volume fraction (f_{vol}), and the power-law slope (α) derived from the square root of the second-order structure functions, fitted over the range 0.5 – 10 pc. The fitting uncertainty (95% confidence level) for all slopes is < 0.02 . Subscripts v , B , and n denote velocity, magnetic field, and density, respectively. For velocity and magnetic fields, scaling slopes are provided for the total (Tot.) field as well as for components parallel (\parallel) and perpendicular (\perp) to the local magnetic field.

**Figure 5.** Distributions of the Stokes parameters I (left), Q (middle), and U (right) for synthetic dust polarization. We consider two distinct frequencies: 353 GHz (top), corresponding to Planck observations, and 150 GHz (bottom), a primary target for future CMB experiments.

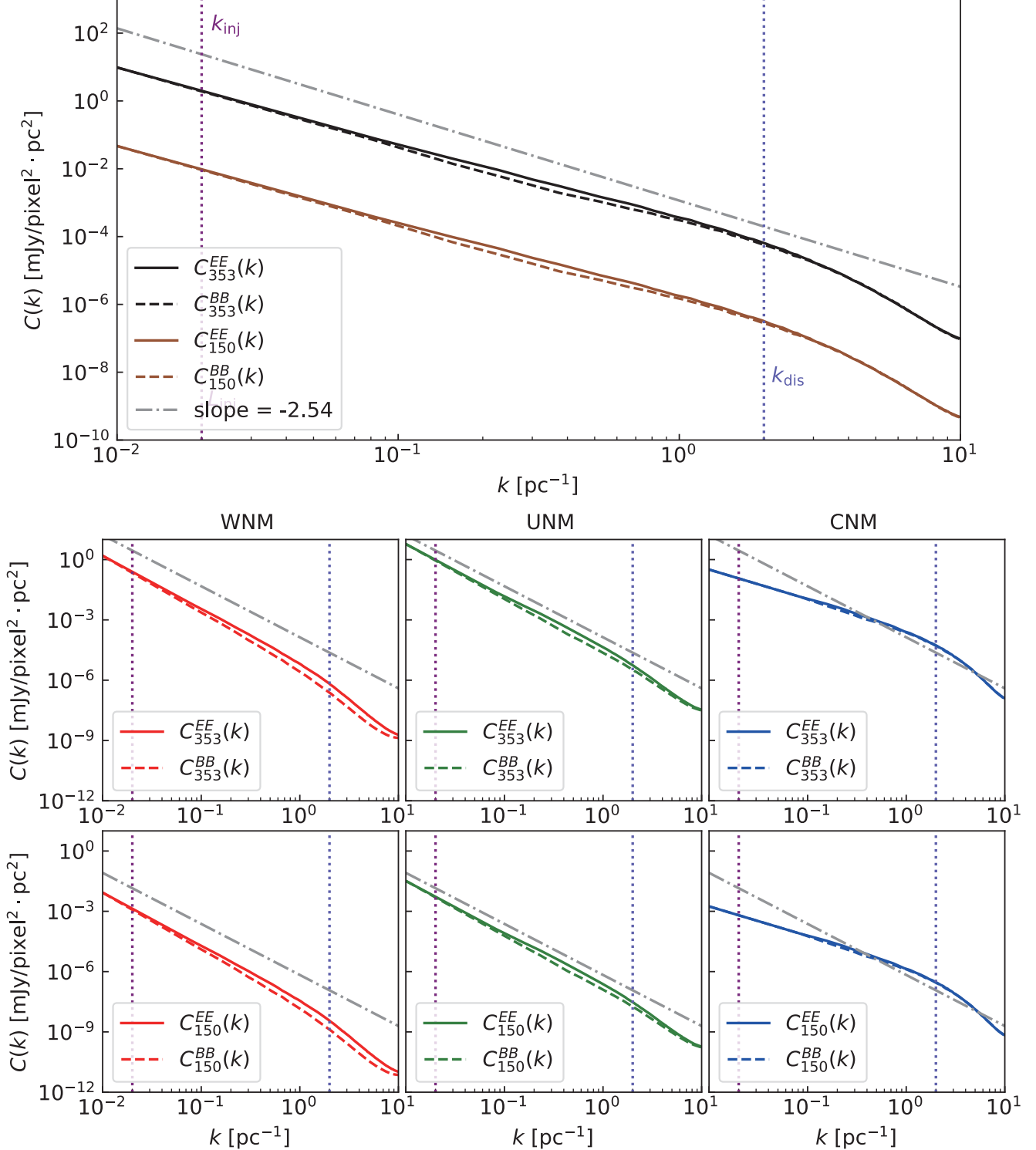


Figure 6. E -mode and B -mode power spectra, C^{EE} and C^{BB} , calculated from synthetic dust polarization. **Top panel:** The power spectra C^{EE} and C^{BB} computed from synthetic dust polarization maps. The gray solid line indicates a reference slope of -2.54 , which was the C^{BB} spectral slope measured by Planck at 353 GHz. The subscripts “353” and “150” represent two distinct frequencies: 353 GHz and 150 GHz. k_{inj} means the injection wavenumber of turbulence and k_{dis} is the numerical dissipation wavenumber. **Bottom panel:** same as the top panel, but for C^{EE} and C^{BB} , calculated from dust polarization in WNM, UNM, and CNM, respectively.

Table 2. Properties of the Multi-phase Medium and Polarization Statistics

Phase	M_s	c_s (km s $^{-1}$)	β_{th}	β_{tur}	Slope α_{EE}^*		Slope α_{BB}^*		Peak C^{EE}/C^{BB}	
					353 GHz	150 GHz	353 GHz	150 GHz	353 GHz	150 GHz
Total	1.27	7.40	0.66	1.98	-2.22 ± 0.02	-2.23 ± 0.02	-2.21 ± 0.04	-2.20 ± 0.04	1.59	1.59
WNM	1.11	8.09	0.66	1.41	-2.78 ± 0.05	-2.78 ± 0.05	-2.98 ± 0.05	-2.98 ± 0.05	2.90	2.89
UNM	1.45	6.38	0.70	2.82	-2.61 ± 0.03	-2.61 ± 0.03	-2.69 ± 0.01	-2.70 ± 0.01	2.05	2.05
CNM	6.66	1.17	0.42	40.25	-1.68 ± 0.07	-1.68 ± 0.06	-1.66 ± 0.05	-1.66 ± 0.05	1.35	1.35

Notes. Columns list the median values for the sonic Mach number (M_s), sound speed (c_s), thermal plasma beta (β_{th}), and turbulent plasma beta (β_{tur}). The spectral slope α^* is fitted within the inertial range ($0.02 \lesssim k \lesssim 2 \text{ pc}^{-1}$), with uncertainties corresponding to the 95% confidence level. Subscripts EE and BB denote the E -mode (C^{EE}) and B -mode (C^{BB}) power spectra, respectively.

3.3. Synthetic dust polarization at 150 GHz and 353 GHz

By post-processing the multi-phase simulation with the radiative transfer code POLARIS, we produced synthetic dust polarization maps, including the intensity I and Stokes parameters Q and U at 150 GHz and 353 GHz. The resulting I , Q , and U maps are presented in Fig. 5.

At a given frequency, the three maps exhibit distinct spatial morphologies. When comparing the two frequencies, the most notable difference is in amplitude: the 150 GHz maps are approximately one order of magnitude fainter than the 353 GHz maps. This difference arises because thermal dust emission scales rapidly with frequency. Furthermore, while the maps at the two frequencies are globally similar in spatial distributions, significant local variations exist. A detailed analysis of polarization properties is presented in Truong et al. (2026, in prep.).

3.3.1. Power spectra of E -mode and B -mode

We compute the power spectra C^{EE} and C^{BB} of E -mode and B -mode polarization assuming a flat 100 pc patch of the sky, following the flat-sky approximation method (e.g., Kritsuk et al. 2018). We first perform a 2D Fast Fourier Transform (FFT) on the spatial Stokes parameters $Q(\mathbf{x})$ and $U(\mathbf{x})$ to obtain their Fourier coefficients $\tilde{Q}(\mathbf{k})$ and $\tilde{U}(\mathbf{k})$. These coefficients are then decomposed into E - and B -modes via a coordinate rotation in Fourier space:

$$\begin{aligned} \tilde{E}(\mathbf{k}) &= \tilde{Q}(\mathbf{k}) \cos 2\phi_{\mathbf{k}} + \tilde{U}(\mathbf{k}) \sin 2\phi_{\mathbf{k}}, \\ \tilde{B}(\mathbf{k}) &= -\tilde{Q}(\mathbf{k}) \sin 2\phi_{\mathbf{k}} + \tilde{U}(\mathbf{k}) \cos 2\phi_{\mathbf{k}}, \end{aligned} \quad (8)$$

where $\phi_{\mathbf{k}} = \arctan(k_y/k_x)$ is the azimuthal angle of the wavevector \mathbf{k} . Finally, the 1D power spectra $C^{EE}(k)$ and $C^{BB}(k)$ are calculated by azimuthally averaging the squared magnitudes $|\tilde{E}(\mathbf{k})|^2$ and $|\tilde{B}(\mathbf{k})|^2$ within concentric annular bins, normalized by the physical area of the simulation domain.

As shown in the top panel of Fig. 6, the B -mode power spectrum C^{BB} at 353 GHz follows a power-law scaling with a best-fit slope of -2.22 (Table 2). While the spectrum at low wavenumbers ($k \leq 0.5 \text{ pc}^{-1}$, corresponding to spatial scales $\geq 20 \text{ pc}$) is steeper and consistent with the reference slope of -2.54 reported by Planck, a distinct flattening emerges at $k \gtrsim 0.5 \text{ pc}^{-1}$. Physically, this scale $\leq 20 \text{ pc}$ likely marks the transition from the diffuse WNM to the clumpy CNM formed.

To identify the origin of this flattening, we decompose the total polarization into contributions from the WNM, UNM, and CNM phases. This is achieved by masking the density field based on local phase temperatures during the generation of synthetic Stokes parameter maps—a valid approach given the optically thin nature of the far-infrared regime. As illustrated in the middle panel of Figure 6, the C^{BB} spectra of the individual phases exhibit markedly different characteristics. The WNM spectrum shows a steep power-law slope of -2.98 , while the UNM spectrum, with a slope of -2.69 , most closely aligns with the Planck reference value. In contrast, the CNM spectrum is significantly flatter, with a slope of -1.66 . This spectral flatness ensures that the CNM dominates the total power at high wavenumbers, thereby driving the flattening feature observed in the total, undecomposed spectrum. A similar trend is observed for the E -mode spectrum C^{EE} , which also exhibits small-scale flattening. Notably, E -mode power consistently exceeds B -mode power ($C^{EE} > C^{BB}$) in the WNM and UNM phases, whereas the two become nearly comparable ($C^{EE} \approx C^{BB}$) in the CNM.

These spectral features remain consistent between 150 GHz and 353 GHz. As illustrated in Fig. 6, the power spectra at both frequencies exhibit remarkably similar small-scale flattening and slope transitions, despite the order-of-magnitude difference in their total amplitudes. While our simulation incorporates spatial variations in dust temperature—ranging from approximately 16 to 20 K—the intrinsic dust properties are kept spatially uniform. The frequency-independent nature of the power spectrum shape suggests

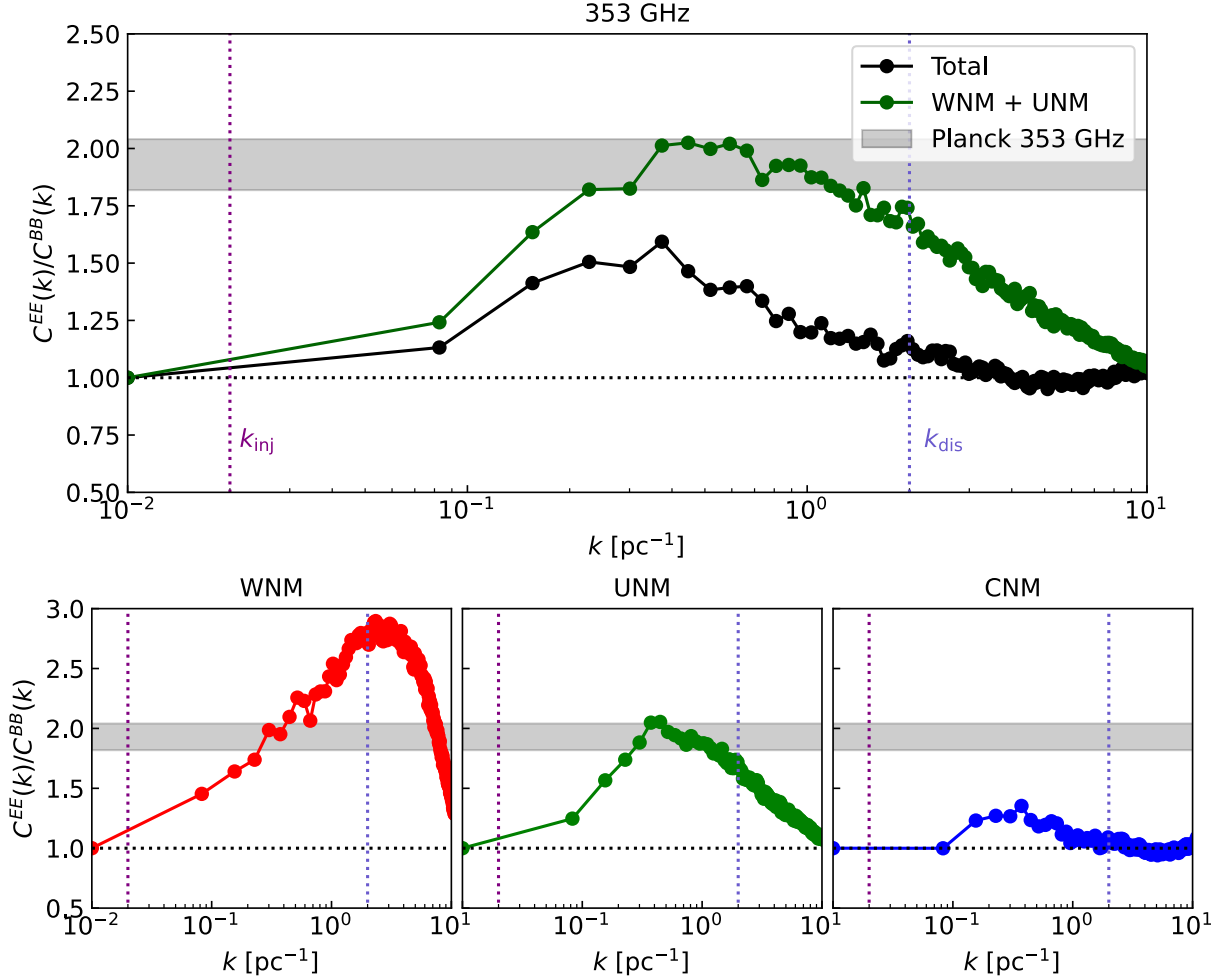


Figure 7. Ratio of C^{EE} to C^{BB} from synthetic dust polarization at 353 GHz. **Top panel:** EE and BB power spectra computed from synthetic dust polarization maps with cold gas ($T < 200$ K) excluded. The shaded gray region denotes the range of C^{EE}/C^{BB} ratios measured by Planck. k_{inj} means the injection wavenumber of turbulence and k_{dis} is the numerical dissipation wavenumber. **Bottom panel:** Same as the top panel, but showing spectra computed separately from different gas phases: WNM ($T > 5000$ K, red), UNM (200 K $< T < 5000$ K, green), and CNM ($T < 200$ K, blue).

that these thermal fluctuations do not introduce significant spectral differences. Consequently, the observed flattening is a direct result of the density fluctuations within the CNM rather than the radiative effects. However, power spectra primarily reflect averaged information globally. Locally, radiative transfer effects may still be significant, leading to frequency-dependent differences in dust emission (see Fig. 5), particularly in regions where multiphase clouds overlap along the line of sight.

3.3.2. EE/BB asymmetry in WNM, UNM, and CNM

Figure 7 displays the power spectrum ratio C^{EE}/C^{BB} across the sampled scales. A prominent feature within the inertial range ($0.02 \lesssim k \lesssim 2 \text{ pc}^{-1}$) is that the ratio consistently exceeds unity. This dominance of E -mode power is a characteristic signature of magnetized anisotropic structure in the ISM. Physically, this asymmetry arises from the

preferred alignment of dust filaments with local magnetic field lines. Such structural alignment creates a geometric anisotropy that projects significantly more power into E -modes than B -modes upon line-of-sight integration.

Our total emission results are qualitatively consistent with Planck observations, which reported a ratio of $EE/BB \approx 2$ (indicated by the gray shaded region). Although our peak value (~ 1.6) is lower than the Planck value, this difference is primarily attributable to the presence of supersonic and super-Alfvénic CNM. Similar reduced ratios (~ 1.5 – 1.6) have been noted in previous numerical studies (Kritsuk et al. 2018; Ho et al. 2025), where insufficient resolution was often cited as a potential cause. However, our resolution study in the Appendix (see Fig. 10) demonstrates that the CNM’s contribution to the EE/BB ratio is well-converged at 2048^3 (~ 0.05 pc). Consequently, we conclude that the lower EE/BB ratio and the associated spectral flattening are phys-

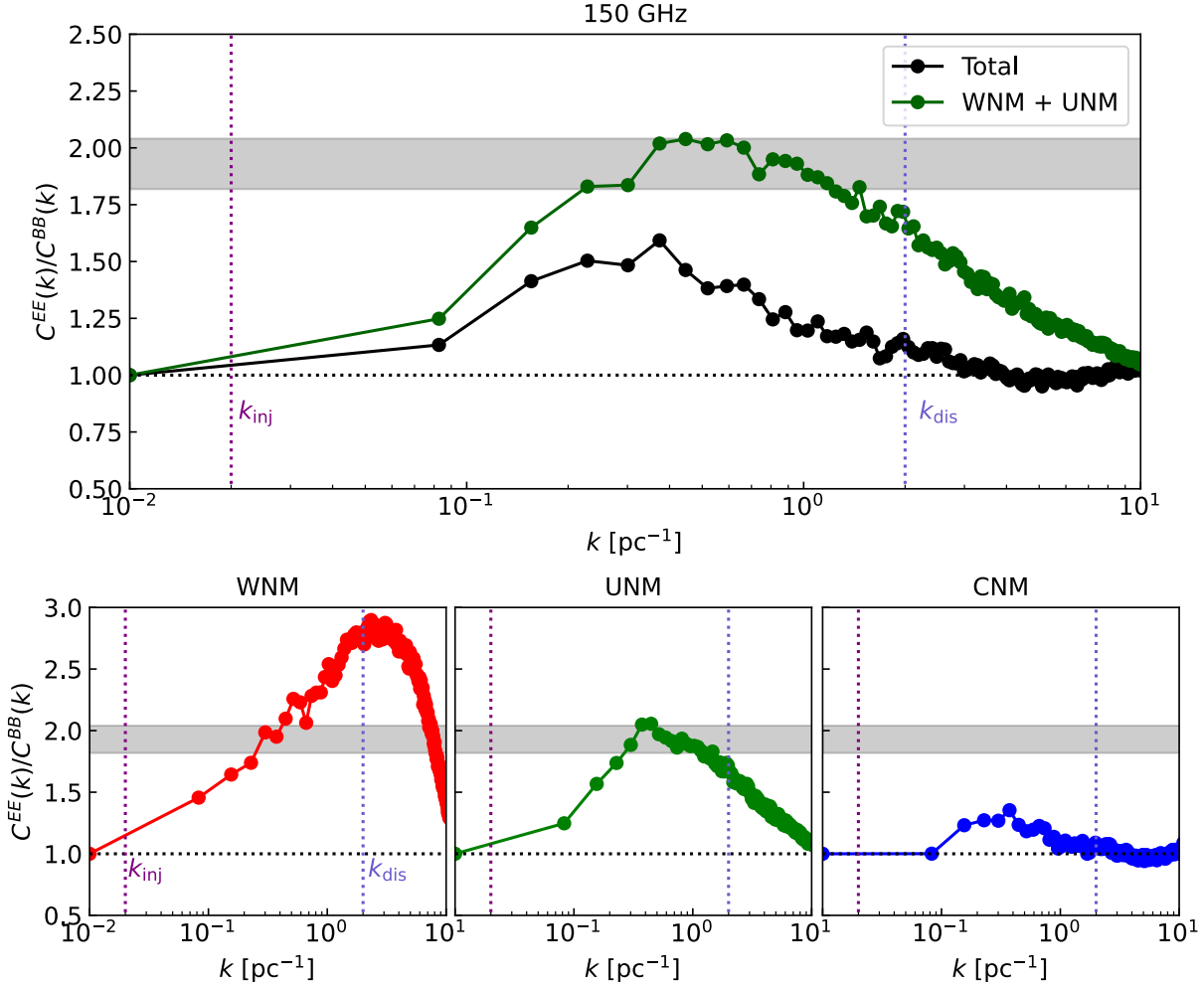


Figure 8. Same as Fig. 7, but at 150 GHz.

ical signatures of shocked, supersonic, and super-Alfvénic turbulence within the CNM phase.

The multi-phase decomposition further elucidates these individual contributions: the WNM polarization yields a high EE/BB ratio peaking at 2.90, while the UNM produces a maximum ratio of ≈ 2.05 , aligning remarkably well with Planck observations. In contrast, the dense CNM yields a significantly lower peak ratio of ≈ 1.35 . Interestingly, excluding the CNM contribution (i.e., considering only the UNM and WNM) results in an aggregate EE/BB ratio of ≈ 2 , a value that persists toward large wavenumbers where the WNM ratio itself exceeds two. Despite its very high ratio at certain wavenumbers, the overall contribution of the WNM to the total power is relatively minor, likely due to its lower density and consequently smaller contribution to the integrated polarization signal. These findings suggest that the UNM, which has the largest mass fraction, could be the dominant contributor to the polarized dust foreground typically observed at high Galactic latitudes.

Furthermore, the EE/BB trends at 150 GHz and 353 GHz exhibit negligible differences, confirming that this asymme-

try is fundamentally driven by the MHD turbulence and remains insensitive to emission frequency in an environment with uniform dust properties. If future observations were to reveal a frequency-dependent EE/BB ratio, it would indicate significant spatial variations in dust intrinsic properties or temperatures.

4. CONCLUSION

In this study, we investigated the physical origin of Galactic dust polarization properties using high-resolution (2048^3) 3D MHD simulations of the turbulent multiphase ISM, coupled with synthetic dust polarization calculations using the POLARIS radiative transfer code. By separating the warm (WNM), unstable (UNM), and cold (CNM) neutral media, we quantified how the distinct turbulence regimes and magnetic field alignments in each phase shape the polarized dust thermal emission at 353 GHz and 150 GHz. Our main findings are summarized as follows:

- Given typical ISM conditions ($B \approx 3 \mu\text{G}$ and $\sigma_v \approx 10 \text{ km s}^{-1}$), we found that the WNM and UNM are globally transonic and trans-Alfvénic ($M_s \sim 1.1\text{--}1.5$,

$\beta_{\text{tur}} \sim 1.4\text{--}2.8$), favoring strong anisotropy in velocity and magnetic field fluctuations with the fluctuations perpendicular to the local magnetic field larger than the parallel component. In contrast, the CNM is isotropic, highly supersonic, and super-Alfvénic ($M_s \approx 6.6$, $\beta_{\text{tur}} \approx 40$), indicating the dominance of turbulent motion, and the magnetic field within the CNM is highly stochastic and tangled. This dynamical distinction is reflected in the velocity structure functions, which exhibit a Kolmogorov-like slope ($\sim 1/3$) in the WNM and steepen to a shock-dominated Burgers scaling ($\sim 1/2$) in the CNM.

2. We found the WNM, UNM, and CNM have distinct statistical scaling of turbulent fluctuations. The square root of the second-order velocity structure function exhibits a Kolmogorov-like slope ($\sim 1/3$) in the WNM and UNM, consistent with subsonic/transonic turbulence⁴. However, in the CNM, this slope steepens to $\sim 1/2$, indicative of shock-dominated Burgers turbulence. Furthermore, while magnetic field fluctuations in the WNM track the velocity scaling, the CNM magnetic field becomes uncorrelated at scales larger than ~ 5 pc. Density structure functions for the dense UNM and CNM are flat, reflecting that density fluctuations in these phases are concentrated at small scales.
3. The spectral slopes of E - and B -modes vary significantly by phase. We found that the dust polarization from UNM yields spectral values close to Planck 353 GHz measurements, while the one from WNM has a steeper spectrum. In contrast, the CNM produces significantly shallower spectra, featuring a noticeable flattening at small scales ($k \gtrsim 0.5 \text{ pc}^{-1}$).
4. Comparing synthetic maps at 150 GHz and 353 GHz, we found that the power spectra exhibit similar flattening behaviors and slope transitions at small scales. These frequency-independent features are primarily driven by the spatial density fluctuations of the CNM rather than temperature or frequency-dependent radiative transfer effects.
5. The trans-Alfvénic WNM and UNM exhibit a tight parallel alignment of density structures with the magnetic field. This alignment yields high EE/BB polarization ratios (≈ 2 for UNM and ≈ 3 for WNM). Conversely, the super-Alfvénic turbulence in the CNM randomizes the magnetic field orientation, resulting in weak alignment and an isotropic EE/BB ratio of ~ 1.3 . Our synthetic observations indicate that dust polarization from the WNM and UNM yields an EE/BB ratio (≈ 2) most consistent with Planck 353 GHz measurements, suggesting it is a dominant contributor to the polarized foreground.

In summary, our results highlight the necessity of accounting for the multiphase nature of the ISM in foreground polarization modeling. The distinct polarization signatures of

the WNM, UNM, and CNM provide a physically motivated framework for improving component separation and cleaning strategies for next-generation CMB B -mode experiments.

1 We thank Alex Lazarian for the helpful discussion. Y.H. ac-
 2 knowledges the support for this work provided by NASA
 3 through the NASA Hubble Fellowship grant No. HST-
 4 HF2-51557.001 awarded by the Space Telescope Science
 5 Institute, which is operated by the Association of Uni-
 6 versities for Research in Astronomy, Incorporated, under
 7 NASA contract NAS5-26555. This work used SDSC Ex-
 8 panse CPU and NCSA Delta CPU and GPU through alloca-
 9 tions PHY230032, PHY230033, PHY230091, PHY230105,
 10 PHY230178, and PHY240183, from the Advanced Cyber-
 11 infrastructure Coordination Ecosystem: Services & Support
 12 (ACCESS) program, which is supported by National Sci-
 13 ence Foundation grants #2138259, #2138286, #2138307,
 14 #2137603, and #2138296. We acknowledge the computa-
 15 tional resources supported by NASA High-End Computing
 16 (HEC), Request (SMD-24-33263831). T.H. and B.T. are sup-
 17 ported by the main research project (No. 2025186902) from
 18 Korea Astronomy and Space Science Institute (KASI). B.T.
 19 acknowledges the use of the gnmnu HPC cluster of KASI for
 20 performing synthetic modeling of thermal dust polarization
 21 and data analysis.

Software: AthenaK (Stone et al. 2024), Python3 (Van Rossum & Drake 2009), ChatGPT (OpenAI 2022)

APPENDIX

A. EFFECT OF BEAM SIZE

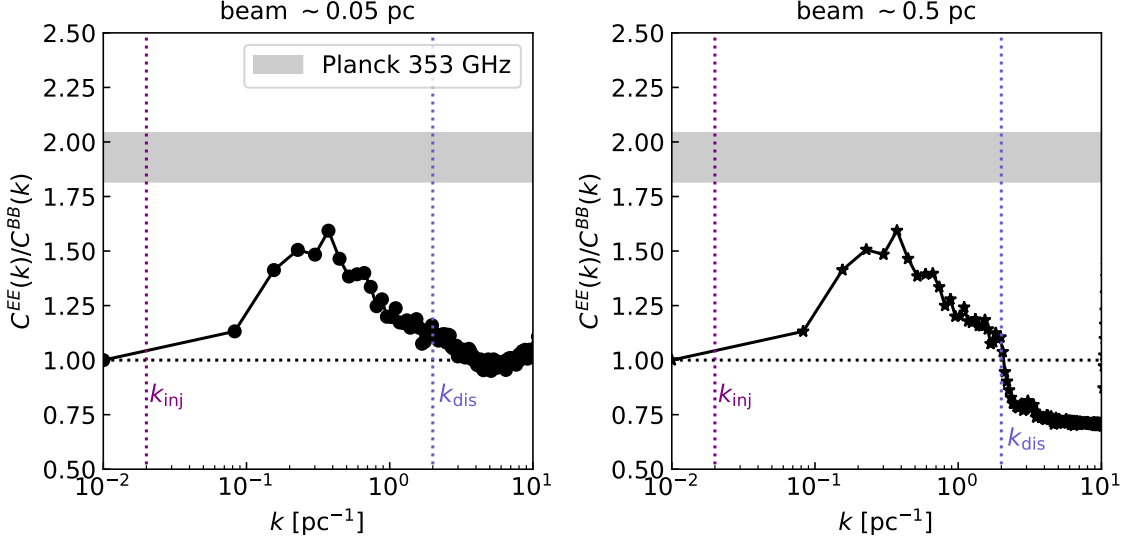


Figure 9. Ratio of C^{EE} to C^{BB} from synthetic dust polarization with all phases included. Two different beam sizes ~ 0.05 pc (left) and ~ 0.5 pc (right) are included. k_{inj} means the injection wavenumber of turbulence and k_{dis} is the numerical dissipation wavenumber.

To evaluate the impact of finite angular resolution on our statistics, we compare the power spectra derived using two distinct beam sizes: ~ 0.05 pc (close to the grid resolution) and ~ 0.5 pc (simulating a coarser observational beam). As illustrated in Fig. 9, the beam smoothing primarily suppresses the power at small scales (high wavenumbers, $k \gtrsim \pi/\theta_{\text{beam}}$), acting effectively as a low-pass filter. Crucially, however, the spectral behaviors and the EE/BB ratio at large scales ($k < k_{\text{beam}}$) remain unaffected.

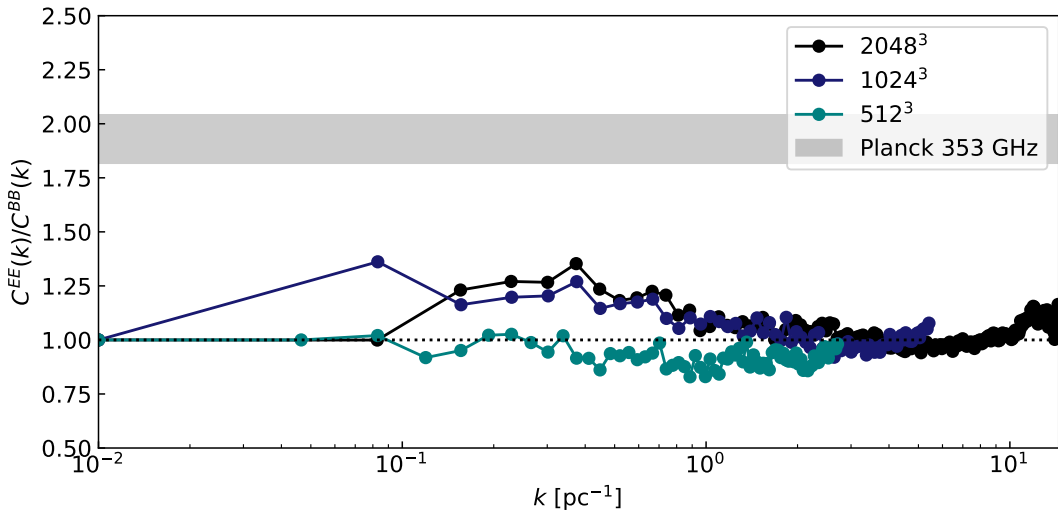


Figure 10. Ratio of C^{EE} to C^{BB} for synthetic 353 GHz dust polarization from CNM. Three different numerical grid resolutions 512^3 , 1024^3 , and 2048^3 are included.

B. RESOLUTION CONVERGENCE

To validate the robustness of the low EE/BB ratio observed in the CNM, we perform a resolution study using three numerical grids: 512^3 , 1024^3 , and 2048^3 . Fig. 9 displays the ratio of C^{EE} to C^{BB} for synthetic dust polarization from CNM at 353 GHz. While the lowest resolution run (512^3) slightly underestimates the ratio, the 1024^3 and 2048^3 simulations show convergence, particularly in the inertial range ($k \gtrsim 0.02 \text{ pc}^{-1}$). Crucially, even at the highest resolution, the maximum ratio is close to 1.3 and distinct from the Planck 353 GHz value of ~ 2 .

REFERENCES

Ade, P., Aguirre, J., Ahmed, Z., et al. 2019, *JCAP*, 2019, 056, doi: [10.1088/1475-7516/2019/02/056](https://doi.org/10.1088/1475-7516/2019/02/056)

Andersson, B. G., Lazarian, A., & Vaillancourt, J. E. 2015, *ARA&A*, 53, 501, doi: [10.1146/annurev-astro-082214-122414](https://doi.org/10.1146/annurev-astro-082214-122414)

Beattie, J. R., & Federrath, C. 2020, *MNRAS*, 492, 668, doi: [10.1093/mnras/stz3377](https://doi.org/10.1093/mnras/stz3377)

BICEP2 Collaboration, Ade, P. A. R., Aikin, R. W., et al. 2014, *PhRvL*, 112, 241101, doi: [10.1103/PhysRevLett.112.241101](https://doi.org/10.1103/PhysRevLett.112.241101)

Boulanger, F., Enßlin, T., Fletcher, A., et al. 2018, *JCAP*, 2018, 049, doi: [10.1088/1475-7516/2018/08/049](https://doi.org/10.1088/1475-7516/2018/08/049)

Brandenburg, A., Bracco, A., Kahnashvili, T., et al. 2019, *ApJ*, 870, 87, doi: [10.3847/1538-4357/aaf383](https://doi.org/10.3847/1538-4357/aaf383)

Chepurnov, A., & Lazarian, A. 2010, *ApJ*, 710, 853, doi: [10.1088/0004-637X/710/1/853](https://doi.org/10.1088/0004-637X/710/1/853)

Cho, J., & Vishniac, E. T. 2000, *ApJ*, 539, 273, doi: [10.1086/309213](https://doi.org/10.1086/309213)

Crutcher, R. M. 2012, *ARAA*, 50, 29, doi: [10.1146/annurev-astro-081811-125514](https://doi.org/10.1146/annurev-astro-081811-125514)

Draine, B. T. 2011, *Physics of the Interstellar and Intergalactic Medium*

Draine, B. T., & Hensley, B. S. 2021, *ApJ*, 919, 65, doi: [10.3847/1538-4357/ac0050](https://doi.org/10.3847/1538-4357/ac0050)

Federrath, C., & Klessen, R. S. 2012, *ApJ*, 761, 156, doi: [10.1088/0004-637X/761/2/156](https://doi.org/10.1088/0004-637X/761/2/156)

Federrath, C., & Offner, S. 2025, arXiv e-prints, arXiv:2510.12203, doi: [10.48550/arXiv.2510.12203](https://doi.org/10.48550/arXiv.2510.12203)

Giang, N. C., Hoang, T., Kim, J.-G., & Tram, L. N. 2023, *MNRAS*, 520, 3788, doi: [10.1093/mnras/stad020](https://doi.org/10.1093/mnras/stad020)

Gray, W. J., & Scannapieco, E. 2017, *ApJ*, 849, 132, doi: [10.3847/1538-4357/aa9121](https://doi.org/10.3847/1538-4357/aa9121)

Ha, T., Li, Y., Kounkel, M., et al. 2022, *ApJ*, 934, 7, doi: [10.3847/1538-4357/ac76bf](https://doi.org/10.3847/1538-4357/ac76bf)

Hensley, B. S., & Draine, B. T. 2023, *The Astrophysical Journal*, 948, 55, doi: [10.3847/1538-4357/acc4c2](https://doi.org/10.3847/1538-4357/acc4c2)

Ho, K. W., Yuen, K. H., Flauger, R., & Kritsuk, A. G. 2025, *PhRvD*, 112, L101302, doi: [10.1103/vhn-33jw](https://doi.org/10.1103/vhn-33jw)

Ho, K. W., Yuen, K. H., & Lazarian, A. 2023, *MNRAS*, 521, 230, doi: [10.1093/mnras/stad481](https://doi.org/10.1093/mnras/stad481)

—. 2024, arXiv e-prints, arXiv:2407.14199, doi: [10.48550/arXiv.2407.14199](https://doi.org/10.48550/arXiv.2407.14199)

Hoang, T. 2025, *ApJ*, 994, 115, doi: [10.3847/1538-4357/ae0a1a](https://doi.org/10.3847/1538-4357/ae0a1a)

Hoang, T., & Lazarian, A. 2008, *MNRAS*, 388, 117, doi: [10.1111/j.1365-2966.2008.13249.x](https://doi.org/10.1111/j.1365-2966.2008.13249.x)

Hoang, T., & Lazarian, A. 2016, *ApJ*, 831, 159

Hoang, T., & Truong, B. 2024, *ApJ*, 965, 183, doi: [10.3847/1538-4357/ad2a56](https://doi.org/10.3847/1538-4357/ad2a56)

Hopkins, P. F. 2025, arXiv e-prints, arXiv:2509.07104, doi: [10.48550/arXiv.2509.07104](https://doi.org/10.48550/arXiv.2509.07104)

Hu, Y. 2025, *ApJ*, 986, 62, doi: [10.3847/1538-4357/add731](https://doi.org/10.3847/1538-4357/add731)

Hu, Y., Lazarian, A., Li, Y., Zhuravleva, I., & Gendron-Marsolais, M.-L. 2020, *ApJ*, 901, 162, doi: [10.3847/1538-4357/abb1c3](https://doi.org/10.3847/1538-4357/abb1c3)

Hu, Y., Scannapieco, E., Buie, II, E., et al. 2025a, *ApJ*, 988, 188, doi: [10.3847/1538-4357/ade701](https://doi.org/10.3847/1538-4357/ade701)

Hu, Y., Stuardi, C., Lazarian, A., et al. 2024, *Nature Communications*, 15, 1006, doi: [10.1038/s41467-024-45164-8](https://doi.org/10.1038/s41467-024-45164-8)

Hu, Y., Whittingham, J., Lazarian, A., et al. 2025b, *ApJ*, 983, 32, doi: [10.3847/1538-4357/adbe68](https://doi.org/10.3847/1538-4357/adbe68)

Hu, Y., Xu, S., & Lazarian, A. 2021, *ApJ*, 911, 37, doi: [10.3847/1538-4357/abea18](https://doi.org/10.3847/1538-4357/abea18)

Hu, Y., Xu, S., Lazarian, A., Stone, J. M., & Hopkins, P. F. 2025c, *ApJ*, 994, 142, doi: [10.3847/1538-4357/ae1127](https://doi.org/10.3847/1538-4357/ae1127)

Hu, Y., Xu, S., Stone, J. M., & Lazarian, A. 2022, *ApJ*, 941, 133, doi: [10.3847/1538-4357/ac9ebc](https://doi.org/10.3847/1538-4357/ac9ebc)

Hu, Y., Yuen, K. H., & Lazarian, A. 2018, *MNRAS*, 480, 1333, doi: [10.1093/mnras/sty1807](https://doi.org/10.1093/mnras/sty1807)

—. 2019a, *ApJ*, 886, 17, doi: [10.3847/1538-4357/ab4b5e](https://doi.org/10.3847/1538-4357/ab4b5e)

Hu, Y., Yuen, K. H., Lazarian, V., et al. 2019b, *Nature Astronomy*, 3, 776, doi: [10.1038/s41550-019-0769-0](https://doi.org/10.1038/s41550-019-0769-0)

Huppenberger, K. M., Rotti, A., & Collins, D. C. 2020, *ApJ*, 899, 31, doi: [10.3847/1538-4357/ab9df9](https://doi.org/10.3847/1538-4357/ab9df9)

Ichiki, K. 2014, *Progress of Theoretical and Experimental Physics*, 2014, 06B109, doi: [10.1093/ptep/ptu065](https://doi.org/10.1093/ptep/ptu065)

Jokipii, J. R. 1966, *ApJ*, 146, 480, doi: [10.1086/148912](https://doi.org/10.1086/148912)

Jokipii, J. R., & Parker, E. N. 1969, *ApJ*, 155, 777, doi: [10.1086/149909](https://doi.org/10.1086/149909)

Kalberla, P. M. W., & Haud, U. 2018, *A&A*, 619, A58, doi: [10.1051/0004-6361/201833146](https://doi.org/10.1051/0004-6361/201833146)

Kalberla, P. M. W., & Kerp, J. 2009, *ARA&A*, 47, 27, doi: [10.1146/annurev-astro-082708-101823](https://doi.org/10.1146/annurev-astro-082708-101823)

Kamionkowski, M., & Kovetz, E. D. 2016, *ARA&A*, 54, 227, doi: [10.1146/annurev-astro-081915-023433](https://doi.org/10.1146/annurev-astro-081915-023433)

Kandel, D., Lazarian, A., & Pogosyan, D. 2018, *MNRAS*, 478, 530, doi: [10.1093/mnras/sty1115](https://doi.org/10.1093/mnras/sty1115)

Koyama, H., & Inutsuka, S.-i. 2002, *ApJL*, 564, L97, doi: [10.1086/338978](https://doi.org/10.1086/338978)

Kritsuk, A. G., Flauger, R., & Ustyugov, S. D. 2018, *PhRvL*, 121, 021104, doi: [10.1103/PhysRevLett.121.021104](https://doi.org/10.1103/PhysRevLett.121.021104)

Krumholz, M. R., Burkhardt, B., Forbes, J. C., & Crocker, R. M. 2018, *MNRAS*, 477, 2716, doi: [10.1093/mnras/sty852](https://doi.org/10.1093/mnras/sty852)

Lagache, G., Haffner, L. M., Reynolds, R. J., & Tufte, S. L. 2000, *A&A*, 354, 247, doi: [10.48550/arXiv.astro-ph/9911355](https://doi.org/10.48550/arXiv.astro-ph/9911355)

Larson, R. B. 1981, *MNRAS*, 194, 809, doi: [10.1093/mnras/194.4.809](https://doi.org/10.1093/mnras/194.4.809)

Lazarian, A., & Hoang, T. 2007, *MNRAS*, 378, 910, doi: [10.1111/j.1365-2966.2007.11817.x](https://doi.org/10.1111/j.1365-2966.2007.11817.x)

Lazarian, A., & Vishniac, E. T. 1999, *ApJ*, 517, 700, doi: [10.1086/307233](https://doi.org/10.1086/307233)

Lazarian, A., & Xu, S. 2021, *ApJ*, 923, 53, doi: [10.3847/1538-4357/ac2de9](https://doi.org/10.3847/1538-4357/ac2de9)

Lazarian, A., & Yuen, K. H. 2018, *ApJ*, 853, 96, doi: [10.3847/1538-4357/aaa241](https://doi.org/10.3847/1538-4357/aaa241)

Lazarian, A., Yuen, K. H., Lee, H., & Cho, J. 2017, *ApJ*, 842, 30, doi: [10.3847/1538-4357/aa74c6](https://doi.org/10.3847/1538-4357/aa74c6)

Lehner, N., & Howk, J. C. 2011, *Science*, 334, 955, doi: [10.1126/science.1209069](https://doi.org/10.1126/science.1209069)

Liu, M., Hu, Y., & Lazarian, A. 2022, *MNRAS*, 510, 4952, doi: [10.1093/mnras/stab3783](https://doi.org/10.1093/mnras/stab3783)

Mathis, J. S., Mezger, P. G., & Panagia, N. 1983, *å*, 128, 212

Mathis, J. S., Rumpl, W., & Nordsieck, K. H. 1977, *Astrophysical Journal*, 217, 425

McClure-Griffiths, N. M., Stanimirović, S., & Rybarczyk, D. R. 2023, *ARA&A*, 61, 19, doi: [10.1146/annurev-astro-052920-104851](https://doi.org/10.1146/annurev-astro-052920-104851)

McKee, C. F., & Ostriker, E. C. 2007, *ARA&A*, 45, 565, doi: [10.1146/annurev.astro.45.051806.110602](https://doi.org/10.1146/annurev.astro.45.051806.110602)

McKee, C. F., & Ostriker, J. P. 1977, *ApJ*, 218, 148, doi: [10.1086/155667](https://doi.org/10.1086/155667)

OpenAI. 2022, Introducing ChatGPT, doi: <https://openai.com/index/chatgpt/>

Planck Collaboration, Abergel, A., Ade, P. A. R., et al. 2014a, *A&A*, 571, A11, doi: [10.1051/0004-6361/201323195](https://doi.org/10.1051/0004-6361/201323195)

—. 2014b, *A&A*, 566, A55, doi: [10.1051/0004-6361/201323270](https://doi.org/10.1051/0004-6361/201323270)

Planck Collaboration, Ade, P. A. R., Aghanim, N., et al. 2015, *A&A*, 576, A105, doi: [10.1051/0004-6361/201424086](https://doi.org/10.1051/0004-6361/201424086)

Planck Collaboration, Adam, R., Ade, P. A. R., et al. 2016a, *A&A*, 586, A133, doi: [10.1051/0004-6361/201425034](https://doi.org/10.1051/0004-6361/201425034)

—. 2016b, *A&A*, 594, A10, doi: [10.1051/0004-6361/201525967](https://doi.org/10.1051/0004-6361/201525967)

Planck Collaboration, Akrami, Y., Ashdown, M., et al. 2020, *A&A*, 641, A11, doi: [10.1051/0004-6361/201832618](https://doi.org/10.1051/0004-6361/201832618)

Putman, M. E., Peek, J. E. G., & Joung, M. R. 2012, *ARA&A*, 50, 491, doi: [10.1146/annurev-astro-081811-125612](https://doi.org/10.1146/annurev-astro-081811-125612)

Qin, G., Matthaeus, W. H., & Bieber, J. W. 2002, *ApJL*, 578, L117, doi: [10.1086/344687](https://doi.org/10.1086/344687)

Reissl, S., Wolf, S., & Brauer, R. 2016, *A&A*, 593, A87, doi: [10.1051/0004-6361/201424930](https://doi.org/10.1051/0004-6361/201424930)

Scoville, N., Lee, N., Vanden Bout, P., et al. 2017, *ApJ*, 837, 150, doi: [10.3847/1538-4357/aa61a0](https://doi.org/10.3847/1538-4357/aa61a0)

Stalpes, K. A., Collins, D. C., & Huffenberger, K. M. 2024, *ApJ*, 972, 26, doi: [10.3847/1538-4357/ad571b](https://doi.org/10.3847/1538-4357/ad571b)

Stanimirović, S., Staveley-Smith, L., Dickey, J. M., Sault, R. J., & Snowden, S. L. 1999, *MNRAS*, 302, 417, doi: [10.1046/j.1365-8711.1999.02013.x](https://doi.org/10.1046/j.1365-8711.1999.02013.x)

Stone, J. M., Mullen, P. D., Fielding, D., et al. 2024, *arXiv e-prints*, arXiv:2409.16053, doi: [10.48550/arXiv.2409.16053](https://doi.org/10.48550/arXiv.2409.16053)

Tress, R. G., Sormani, M. C., Girichidis, P., et al. 2024, *A&A*, 691, A303, doi: [10.1051/0004-6361/202450035](https://doi.org/10.1051/0004-6361/202450035)

Truong, B., & Hoang, T. 2025, *The Astrophysical Journal*, 981, doi: [10.3847/1538-4357/adb423](https://doi.org/10.3847/1538-4357/adb423)

Van Rossum, G., & Drake, F. L. 2009, *Python 3 Reference Manual* (Scotts Valley, CA: CreateSpace)

Vázquez-Semadeni, E. 2025

Vázquez-Semadeni, E., Gazol, A., & Scalo, J. 2000, *ApJ*, 540, 271, doi: [10.1086/309318](https://doi.org/10.1086/309318)

Velguth, B. N., Li, Y., Ha, T., et al. 2025, *ApJ*, 990, 165, doi: [10.3847/1538-4357/adf5c0](https://doi.org/10.3847/1538-4357/adf5c0)

Whittingham, J., Sparre, M., Pfrommer, C., & Pakmor, R. 2023, *MNRAS*, 526, 224, doi: [10.1093/mnras/stad2680](https://doi.org/10.1093/mnras/stad2680)

Wolfire, M. G., Hollenbach, D., McKee, C. F., Tielens, A. G. G. M., & Bakes, E. L. O. 1995, *ApJ*, 443, 152, doi: [10.1086/175510](https://doi.org/10.1086/175510)

Wolfire, M. G., McKee, C. F., Hollenbach, D., & Tielens, A. G. G. M. 2003, *ApJ*, 587, 278, doi: [10.1086/368016](https://doi.org/10.1086/368016)

Xu, S., Ji, S., & Lazarian, A. 2019, *ApJ*, 878, 157, doi: [10.3847/1538-4357/ab21be](https://doi.org/10.3847/1538-4357/ab21be)

Xu, S., & Lazarian, A. 2020, *ApJ*, 894, 63, doi: [10.3847/1538-4357/ab8465](https://doi.org/10.3847/1538-4357/ab8465)

Zaldarriaga, M. 2001, *PhRvD*, 64, 103001, doi: [10.1103/PhysRevD.64.103001](https://doi.org/10.1103/PhysRevD.64.103001)